Turbulence in ferrofluids in channel flow with steady and oscillating magnetic fields

Kristopher R. Schumacher, James J. Riley, and Bruce A. Finlayson

Turbulence in ferrofluids in channel flow with steady and oscillating magnetic fields

Kristopher R. Schumacher*
Department of Chemical Engineering, University of Washington, Seattle, WA 98195

James J. Riley
Department of Mechanical Engineering, University of Washington, Seattle, WA 98195

Bruce A. Finlayson[†]
Department of Chemical Engineering, University of Washington, Seattle, WA 98195

ABSTRACT

The turbulent flow of a ferrofluid in channel flow is studied using direct numerical simulation (DNS). The method of analysis is an extension of that used for Newtonian fluids, with additional features necessary to model the ferrofluid. The analysis is applied to low Reynolds number turbulence in the range of existing experimental data in a capillary. For steady and oscillating magnetic fields, comparisons are made between a Newtonian fluid and a ferrofluid by comparing the pressure drop, turbulent Reynolds number, turbulent kinetic energy, Reynolds stress, velocity and spin profiles. The results are also compared with predictions of a k-ε model to show the accuracy of that model when applied to ferrofluids.

* Present address: Midwest Research Institute, 425 Volker Boulevard, Kansas City, MO 64110
[†] Corresponding author: finlayso@u.washington.edu

I. INTRODUCTION

Ferrofluids are composed of nano-sized particles of a magnetic material and are studied here while flowing in turbulent flow. While most of the applications of ferrofluids have been for laminar flow, they have been considered for enhanced heat transfer in oil-cooled electromagnetic equipment, transducers, and to mix and homogenize a suspension [1,2,3]. Schumacher, *et al.* [4] measured flow properties for a ferrofluid in laminar and turbulent flow in a pipe. They successfully modeled the flow using a k-ε model of turbulence. Zablockis, *et al.* [5] used a two-equation k-ω model of turbulence when studying thermal convection. The present paper is the third in a series to justify the turbulence models by comparison with direct numerical simulation (DNS). The equations governing them in turbulent flow are described more fully in Schumacher, *et al.* [6], where the effect of steady magnetic fields is examined in homogeneous turbulence. A second paper [7] extends this work to homogeneous turbulence with an oscillating magnetic field. The current paper considers channel flow with either a steady or oscillating magnetic field. Wall-bounded flows are more complex than homogeneous flows. The solid boundary makes the flow inhomogeneous and leads to turbulence structures such as wall streaks and bursts and hairpin vortices near the center of the channel. In addition, predictions made here using direct numerical simulation are compared with those from a standard *k*-ε model.

The domain and geometry of the parallel plate channel system is shown in Figure 1. The fluid is driven by a pressure gradient in the *x*-direction. The stream-wise direction is parallel to the mean pressure drop. The wall normal direction is perpendicular to the two parallel walls. The span-wise direction is perpendicular to the streamwise direction and parallel to the two walls. Here, (*x,y,z*) and (*u,v,w*) are used as the streamwise, spanwise, and wall normal coordinates and velocities, respectively. The *x* and *y*-directions are homogeneous, and the dependent variables have periodic boundary conditions in these directions. The *x*-*y* plane is referred to as the homogeneous plane. The direct numerical simulation techniques for solving for Newtonian fluid flows in this geometry are established [8-10]. The literature concludes that the turbulent Newtonian fluid simulation results compare very well with experimental data.

In experimental studies of 'drag-reducing' turbulent polymer flow, the total shear stress is not equal to the sum of the usual shear stress $\mu(\partial\overline{u}/\partial y)$ and the Reynolds shear stress $-\overline{u'v'}$ [11-13]. The difference between the total shear stress and the sum of $\mu(\partial\overline{u}/\partial y)$ and $-\overline{u'v'}$ is called the stress deficit.

In these polymer flow studies, the stress deficit is attributed to viscoelastic properties of the polymer solution. In ferrofluid flow, the total shear stress isn't equal to $\mu(\partial \overline{u}/\partial y) - \overline{u'v'}$ either. Ferrofluid theory suggests that this inequality is due to an asymmetric stress tensor rather than viscoelasticity. In this paper we present 'stress-deficit' profiles that are just the asymmetric Reynolds shear stress. In steady and slowly oscillating magnetic fields, we expect that the total shear stress will be greater than that for an analogous Newtonian fluid.

II. EQUATIONS

The equations are used in a non-dimensionalized form. The characteristic length used is the channel half-width, δ, and the characteristic velocity is chosen to be the friction velocity, $u_\tau = \sqrt{\tau_w^s/\rho}$, where τ_w^s is the symmetric part of the viscous wall stress. The characteristic time is δ/u_τ; the characteristic spin rate is u_τ/δ. The magnetization, $\mathbf{M}$, and magnetic field, $\mathbf{H}$, have the SI units of A/m, and both are normalized by the saturation magnetization, M_{sat}. The normalized governing equations are then the non-dimensional form of equations (2.3, 2.21, and 2.11) of Schumacher, *et al.* [6]:

$$\frac{\partial \mathbf{u}}{\partial t} = -\nabla P' + \frac{1}{\mathrm{Re}_\tau}\nabla^2\mathbf{u} + \mathbf{u}\times(\nabla\times\mathbf{u}) + \left(\frac{\Delta P}{L}\right)\left(\frac{\delta}{\rho u_\tau^2}\right)\mathbf{e}_x + \frac{C_\zeta}{\mathrm{Re}_\tau}\nabla\times(2\boldsymbol{\omega}-\nabla\times\mathbf{u}) + C_{MBF}\mathbf{M}\cdot\nabla\mathbf{H}$$

$$\frac{\partial \mathbf{M}}{\partial t} = -\mathbf{u}\cdot\nabla\mathbf{M} + \boldsymbol{\omega}\times\mathbf{M} - \frac{1}{C_{\tau_B}}\left(\mathbf{M}-\mathbf{M}_{eq}\right)$$

$$\nabla\cdot\mathbf{u} = 0, \quad \nabla\times\mathbf{H} = 0, \quad \nabla\cdot(\mathbf{H}+\mathbf{M}) = 0, \quad \boldsymbol{\omega} = 1/2\,\nabla\times\mathbf{u} - C_{TRQ}\mathbf{M}\times\mathbf{H}$$

for the momentum, magnetization, continuity, Maxwell, and spin equations, respectively. The magnetization equation was derived by Shliomis [14] and is used here in a normalized version. The rotational form of the momentum equation is used here because it conserves energy to machine precision for our type of spatial discretization methods [15]. The parameters in the above equations are:

$$\mathrm{Re}_\tau = \frac{\delta u_\tau}{\nu}, \quad C_\zeta = \zeta/\mu, \quad C_{MBF} = \frac{\mu_o M_{sat}^2}{\tau_w^s}, \quad C_{\tau_B} = \frac{1}{\mathrm{Re}_\tau}\frac{\tau_w^s \tau_B}{\mu}, \quad C_{TRQ} = \tfrac{1}{4}\left(\mathrm{Re}_\tau\frac{C_{MBF}}{C_\zeta}\right)$$

An overall force balance on the system gives

$$\Delta P/L = \tau_w/\delta, \tag{1}$$

where τ_w is the total viscous stress at the wall. The total viscous stress in a ferrofluid is composed of a symmetric and an asymmetric part,

$$\tau_w = \tau_w^s + \tau_w^a. \tag{2}$$

Using Eqns. (1-2), along with the definition of u_τ, the stream-wise pressure body force term in the normalized momentum equation becomes

$$\left(\frac{\Delta P}{L}\right)\left(\frac{\delta}{\rho u_\tau^2}\right)\mathbf{e}_x = \left(1+\frac{\tau_w^a}{\rho u_\tau^2}\right)\mathbf{e}_x. \tag{3}$$

Using Eqn. (3) the normalized momentum equation is

$$\frac{\partial \mathbf{u}}{\partial t} = -\nabla P' + \frac{1}{\mathrm{Re}_\tau}\nabla^2\mathbf{u} + \mathbf{u}\times(\nabla\times\mathbf{u}) + \left(1+\frac{\tau_w^a}{\rho u_\tau^2}\right)\mathbf{e}_x + \frac{C_\zeta}{\mathrm{Re}_\tau}\nabla\times(2\boldsymbol{\omega}-\nabla\times\mathbf{u}) + C_{MBF}\mathbf{M}\cdot\nabla\mathbf{H}$$

When $C_\zeta = 0$, $C_{MBF} = 0$, and $\tau_w^a = 0$, the momentum equations revert to the classical Navier-Stokes form.

It is common in the turbulent channel flow DNS literature to eliminate the pressure from the equations, and that is done here. This step allows continuity to be satisfied automatically and requires less memory since P' doesn't have to be stored. To eliminate pressure, P', the momentum equations are recast into a velocity-vorticity formulation with the same general form as the starting equations used by Kim *et al.* [8]. First, taking the divergence of the momentum equation, and using continuity, yields the Poisson equation for pressure,

$$\nabla^2 P' = \nabla\cdot\mathbf{F} \quad \text{where } \mathbf{F} = \mathbf{u}\times(\nabla\times\mathbf{u}) + C_\zeta/\mathrm{Re}_\tau\nabla\times(2\boldsymbol{\omega}-\nabla\times\mathbf{u}) + C_{MBF}\mathbf{M}\cdot\nabla\mathbf{H}.$$

Then, apply the Laplacian operator to the wall normal component of the momentum equation, and use the Poisson equation to eliminate pressure; the result is a fourth order equation for the wall-normal velocity, w,

$$\frac{\partial \nabla^2 w}{\partial t} = \frac{1}{\mathrm{Re}_\tau} \nabla^4 w + h_3 \tag{4}$$

where $h_3 = -\partial/\partial z \left(\partial F_1/\partial x + \partial F_2/\partial y\right) + \left(\partial^2/\partial x^2 + \partial^2/\partial y^2\right) F_3$. Eqn. (4) has boundary conditions $w(z \pm 1) = 0$ and $\partial w/\partial z (z \pm 1) = 0$. To avoid dealing directly with a biharmonic operator, Eqn. (4) is split into two second-order equations

$$\frac{\partial \phi}{\partial t} = \frac{1}{\mathrm{Re}_\tau} \nabla^2 \phi + h_3 \tag{5}$$
$$\nabla^2 w = \phi. \tag{6}$$

Together, these two equations must satisfy the $w(z \pm 1) = 0$ and $\partial w/\partial z (z \pm 1) = 0$ boundary conditions. The curl of the momentum equation yields equations for the components of vorticity. The equation for the wall-normal component of vorticity, $g = \partial v/\partial x - \partial u/\partial y$, is

$$\frac{\partial g}{\partial t} = \frac{1}{\mathrm{Re}_\tau} \nabla^2 g + h_g \text{ where } h_g = \partial F_2/\partial x - \partial F_1/\partial y. \tag{7}$$

The boundary condition of normal vorticity at the wall is $g(z \pm 1) = 0$.

Eqn. (5-7) are the form of the momentum equations that we advance in time. The general form is the same as used by Kim, *et al.* [8]; the major difference lies in the definition of F. In the Navier-Stokes formulation by Kim, *et al.* [8], $\mathbf{F} = \mathbf{u} \times (\nabla \times \mathbf{u})$.

III. NUMERICAL METHOD

A. Fractional pressure drop

Turbulent channel flow with a constant mass flow rate is simulated by dynamically adjusting Re_τ after each time step such that the bulk average velocity is equal to some specified constant value. The numerical experiment is designed to study the fractional pressure drop of ferrofluid under the influence of a uniform axial magnetic field. The fractional pressure drop (P_{FPD}) is the pressure drop required to maintain a constant flow rate in a magnetic field divided by the ΔP required to maintain the same flow rate without a magnetic field, minus one:

$$P_{FPD} = \frac{\Delta P(H)}{\Delta P(0)} - 1$$

The homogeneous simulations of Schumacher, *et al* [6,7], and the *k-ε* simulations of Schumacher et al. [4], suggest that the ferrofluid behaves like a Newtonian fluid when the magnetic field is absent. Therefore, we use ΔP_o from the Newtonian fluid simulations to approximate $\Delta P(0)$.

$$P_{FPD} = \frac{\Delta P(H)}{\Delta P_o} - 1,$$

where the subscript o refers to the Newtonian fluid. The fractional pressure drop is computed from the normalized simulation data using

$$P_{FPD} = \left(1 + \frac{\tau_w^a}{\rho u_\tau^2}\right)\frac{Re_\tau^2}{Re_{\tau_o}^2} - 1,$$

where the derivation is given in Schumacher [16, Appendix D].

B. Solution for ϕ, g and velocity normal to the wall

The equations for ϕ and g are advanced in time using a semi-implicit technique. The diffusive terms are treated implicitly with the Crank-Nicholson method, and all other terms, including the non-linear terms, are treated explicitly with the Adams-Bashforth method. The time discretized equations are

$$\left(1-\frac{\Delta t}{2\,\mathrm{Re}_\tau}\nabla^2\right)\phi^{n+1}=\phi_{RHS} \qquad (8)$$

$$\left(1-\frac{\Delta t}{2\,\mathrm{Re}_\tau}\nabla^2\right)g^{n+1}=g_{RHS} \qquad (9)$$

where

$$\phi_{RHS}=\left(1+\frac{\Delta t}{2\,\mathrm{Re}_\tau}\nabla^2\right)\phi^n+\Delta t\left(\alpha h_3^{\;n}+\beta h_3^{\;n-1}\right),\quad g_{RHS}=\left(1+\frac{\Delta t}{2\,\mathrm{Re}_\tau}\nabla^2\right)g^n+\Delta t\left(\alpha h_g^{\;n}+\beta h_g^{\;n-1}\right).$$

A low storage third order Runge-Kutta method is used for the first time step in order to "start" the Adams-Bashforth scheme. If the Δt changes to meet stability requirements, the first step after the change is advanced using the Runge-Kutta method in order to "restart" the Adams-Bashforth method at a new Δt.

The Courant number for this flow, $C_N=\pi\Delta t\{|u/dx|+|v/dy|+|w/dz|\}_{\max}$, limits the maximum stable time-step size. With the Adams-Bashforth-Crank-Nicolson (ABCN) method, the simulation is stable as long as $C_N<1$ [10].

Boundary conditions for ϕ do not exist. Thus, the direct solution of Eqn. (5) and subsequent calculation of a w that satisfies $w(z\pm1)=0$ and $\partial w/\partial z(z\pm1)=0$ is not possible. To get an updated value of normal velocity that satisfies these boundary conditions, we use the same technique as Kim *et al.* [8] and let

$$w^{n+1}=w_p^{n+1}+c_1 w_1^{n+1}+c_2 w_2^{n+1} \qquad (10)$$

where w_p^{n+1}, is the particular solution, and w_1^{n+1} and w_2^{n+1}, are the two homogeneous solutions. The w_p^{n+1}, w_1^{n+1}, and w_2^{n+1} are computed as [8]:

$$\left(1-\frac{\Delta t}{2\,\mathrm{Re}_\tau}\nabla^2\right)\phi_p^{\;n+1}=\phi_{RHS},\quad \phi_p^{\;n+1}(\pm1)=0,\quad \nabla^2 w_p^{\;n+1}=\phi_p^{\;n+1},\quad w_p^{\;n+1}(\pm1)=0$$

$$\left(1-\frac{\Delta t}{2\,\mathrm{Re}_\tau}\nabla^2\right)\phi_1^{n+1}=0\,,\qquad \phi_1^{n+1}(+1)=0,\ \phi_1^{n+1}(-1)=1,\qquad \nabla^2 w_1^{n+1}=\phi_1^{n+1},\qquad w_1^{n+1}(\pm1)=0$$

$$\left(1-\frac{\Delta t}{2\,\mathrm{Re}_\tau}\nabla^2\right)\phi_2^{n+1}=0\qquad,\qquad \phi_2^{n+1}(+1)=1,\ \phi_2^{n+1}(-1)=0,\qquad \nabla^2 w_2^{n+1}=\phi_2^{n+1},\qquad w_2^{n+1}(\pm1)=0.$$

The constants c_1 and c_2 in Eqn. (10) are then chosen such that the Neumann condition on the normal velocity is satisfied. The constants are found by evaluating

$$\begin{vmatrix} c_1 \\ c_2 \end{vmatrix}=-G^{-1}b\,,$$

where $G^{-1}=\begin{bmatrix} \left.\dfrac{dw_1^{n+1}}{dz}\right|_{z=+1} & \left.\dfrac{dw_2^{n+1}}{dz}\right|_{z=+1} \\[2ex] \left.\dfrac{dw_1^{n+1}}{dz}\right|_{z=-1} & \left.\dfrac{dw_2^{n+1}}{dz}\right|_{z=-1} \end{bmatrix}^{-1}$ and $b=\begin{bmatrix} \left.\dfrac{dw_p^{n+1}}{dz}\right|_{z=+1} \\[2ex] \left.\dfrac{dw_p^{n+1}}{dz}\right|_{z=-1} \end{bmatrix}.$

G^{-1} is the Greens function matrix. For a given time step, Δt, the w_1^{n+1}, w_2^{n+1}, and G^{-1} are computed once, and saved in memory.

A spectral method using Fourier series in the homogeneous directions and a Chebyshev expansion in the wall-normal direction is used for spatial discretization. The domain transforms from (x,y,z) to (k_x, k_y, z). Derivatives in homogeneous directions are evaluated in Fourier space by multiplication by an appropriate wave number, while derivatives in the normal direction are computed using Chebyshev collocation matrices. After the transformation, the governing equations can be solved for each wave-number pair (k_x, k_y). Non-linear terms are computed in physical space, and then the products are transformed back to Fourier space. The Fourier transformed products are completely de-aliased using the 2/3 truncation method.

Following the notation of Rutledge and Sleicher [10], the transformed Eqns. (6, 8, 9), are discretized and written in matrix notation as

$$\left[B_{ij} - cI_{ij}\right]\hat{g}_j^{n+1} = -\frac{1}{f_c}\hat{g}_{RHS_i}, \tag{11}$$

$$\left[B_{ij} - cI_{ij}\right]\hat{\phi}_j^{n+1} = -\frac{1}{f_c}\hat{\phi}_{RHS_i}, \tag{12}$$

$$\left[B_{ij} - c_w I_{ij}\right]\hat{w}_j^{n+1} = \hat{\phi}_i^{n+1}, \tag{13}$$

where **B** is the second-derivative collocation array, **I** is the identity matrix, and

$$c = 1/f_c + k_1^2 + k_2^2, \quad c_w = k_1^2 + k_2^2, \quad f_c = \Delta t/(2\,\mathrm{Re}_\tau), \quad i = 0 \ to \ N_3 \ \text{and} \ j = 0 \ to \ N_3.$$

To apply the boundary conditions, the first and last columns of the collocation array are multiplied by the boundary condition and then brought to the RHS. The first and last rows of the collocation array are then not necessary. Eqn. (11-13) are then written as

$$\left[B_{ij} - cI_{ij}\right]\hat{g}_j^{n+1} = -\frac{1}{f_c}\hat{g}_{RHS_i} - B_{ik}\hat{g}_k^{n+1},$$

$$\left[B_{ij} - cI_{ij}\right]\hat{\phi}_j^{n+1} = -\frac{1}{f_c}\hat{\phi}_{RHS_i} - B_{ik}\hat{\varphi}_k^{n+1},$$

$$\left[B_{ij} - c_w I_{ij}\right]\hat{w}_j^{n+1} = \hat{\phi}_i^{n+1} - B_{ik}\hat{w}_k^{n+1}, \ i = 1 \ to \ N_3 - 1 \ \text{and} \ j = 1 \ to \ N_3 - 1, \ \text{and} \ k = 0 \ and \ N_3.$$

These equations are unique for each wavenumber pair, and c and c_w are functions of wavenumber; c is also a function of Δt. In our solution, we compute the inverse $\left[B_{ij} - cI_{ij}\right]^{-1}$ and $\left[B_{ij} - c_w I_{ij}\right]^{-1}$ at each wave number pair and save these in memory to reduce the computation time. If Δt is changed, the inverse values of the inverse arrays must be recomputed and re-saved in memory.

In solving this system of Helmholtz equations, one must be careful that the c and c_w values lie within the range of eigenvalues of **B**. The maximum eigenvalue of **B** is given for different values of N_z in Table I. The maximum value of c increases as the grid is refined, in the homogeneous directions, and as Δt is decreased.

C. Solve for *u* and *v*

The homogeneous velocity components, *u* and *v*, are computed using

$$\ddot{\hat{u}} = \frac{ik_y\ddot{\hat{g}}_z^{n+1} + ik_x D\ddot{\hat{w}}^{n+1}}{k^2} \text{ and } \ddot{\hat{v}} = \frac{-ik_x\ddot{\hat{g}}_z^{n+1} + ik_y D\ddot{\hat{w}}^{n+1}}{k^2}. \tag{14}$$

The $\hat{u}$ and $\hat{v}$ in Eqn. (14) are derived in Schumacher [16, Appendix E].

D. Solve for the magnetic field and magnetization

The mean magnetic field within the domain is related to the externally applied magnetic field. In our specific system, the average internal magnetic field is related to the external field by:

$$\hat{H}_{x\ (0,0,z)} = \hat{H}_{o_x}\cos(\Omega t), \quad \hat{H}_{y\ (0,0,z)} = 0, \text{ and } \quad \hat{H}_{z\ (0,0,z)} + \hat{M}_{z\ (0,0,z)} = \hat{B}_{o_z}\big/\mu_o. \tag{15}$$

The relationships in Eqn. (15) are enforced by direct substitution into the (0,0) Fourier modes.
Due to the chaotic behavior of the flow field and the coupling between the velocity, magnetization, and magnetic field, the magnetization and magnetic field will have a spectrum of fluctuating components. Maxwell's equations are used to relate the fluctuating magnetic field with the fluctuating magnetization at an instant in time and are solved as shown in Schumacher, *et al.* [6]. ϕ can be computed by solving the Poisson equation $\nabla^2\phi = -\nabla\cdot\mathbf{M}$. This equation is solved for $\hat{\phi}$ in Fourier space by solving the following Helmholtz equation

$$\left[D^2 - c_w I\right]\hat{\phi}(z) = -ik_i\hat{M}_i(z),$$

where $c_w = k_x^2 + k_y^2$. Once $\hat{\phi}$ is known, the components of $\hat{\mathbf{H}}$ are computed.

In the channel flow simulations the Shliomis magnetization equation [14 and Eq. (2.21) in Schumacher 6] is used and the magnetic convection term, found to be very small in Part II, is ignored. The magnetization equation is updated in physical space and then transformed back into Fourier space, where it is dealiased using the 2/3-truncation method. The full Shliomis magnetization equation is

$$\frac{\partial M_i}{\partial t} = -\{u \cdot \nabla M\}_i + \{\omega \times M\}_i - \frac{1}{C_{\tau_B}}(M_i - M_{eq_i}). \tag{16}$$

The equilibrium magnetization is related to the magnetic field by the non-linear function

$$M_{eq_i} = \chi H_i, \quad \text{where} \quad \chi = \frac{M_S}{H}\left(\frac{1}{\tanh(\xi)} - \frac{1}{\xi}\right), \quad \xi = \frac{\mu_o m H}{k_B T}, \text{ and } H = \sqrt{H_x^2 + H_y^2 + H_z^2}.$$

A semi-implicit time stepping method is used. The M/C_{τ_B} term is treated implicitly and the nonlinear terms and equilibrium magnetization term are treated explicitly. An Euler/backward-Euler or Adams-Bashforth/Crank-Nicolson semi-implicit scheme is used.

There is theoretical evidence [17-20] that under certain conditions on vorticity, magnetic field, and oscillation frequency the flow solutions in laminar flow may be unstable or multi-valued. The parameter ξ, identifies the strength of the magnetic field.

$$\xi = \frac{\mu_o m H_{ox}}{k_B T},$$

where μ_0 is the permeability of free space, m is the magnetic moment of a single particle, k_B is Boltzmann's constant and T is the absolute temperature. The instabilities occur for large $\xi = 10\text{-}120$, but only values up to 5.76 are used here. In addition, the largest value of $\tau_B\Omega$ is 0.1, whereas values up to 5 are needed for the unusual effects to be predicted theoretically. In that case other magnetization equations are needed [21-22]. In the cases studied here, though, the parameters are not in the problematic range, and previous simulations [7] indicate that for the parameters studied here the Felderhof and Kroh [21] and Martsensuk, *et al.* [22] magnetization equation make little difference compared with the one used here.

E. Solve for spin

The torque is computed spectrally and dealiased using the 2/3-truncation method. Once the torque is computed using the updated **M** and **H** values, the spin can be calculated using the spin equation.

$$\boldsymbol{\omega}^{n+1} = 1/2\nabla \times \mathbf{u}^n - C_{TRQ}\mathbf{M}^{n+1} \times \mathbf{H}^{n+1}$$

F. Calculation order

The order in which we update the set of equations is as follows. First, the magnetization equation is advanced one time step. Using the updated magnetization, the magnetic field is then updated in time. Next, using the old velocity field and the new **M** and **H**, the spin is computed. The momentum equation is then updated using the new values of **M**, **H**, and spin. Finally, after the momentum equation is updated, the spin is recomputed using the new velocity field. Solving the spin equation twice, before and after the velocity update, helped stabilize the simulation.

The turbulent flows of interest have Reynolds numbers of 2250 and 2800. For all cases, the system domain size is $4\pi\delta(4/3\pi\delta)(2\delta)\ L_xL_yL_z$. The simulations with Reynolds number = 2250 use 144 x 144 x 65 physical space grid points, and the simulations with Reynolds number = 2800 use 192 x 160 x 65 grid points. The domain size, grid spacing, and time step size, for our cases, are all comparable with what has been reported in the literature for low Reynolds numbers [9, 10, 23, 24].

Table II lists the cases solved. Cases A and H are Newtonian fluid cases. Parameters varied include the Reynolds number, magnetic field (specified by the parameter ξ), and frequency of oscillation, Ω.

The range of c and c_w, in the Helmholtz equations varies with grid resolution and Δt. Based on the range of c for our problem, we choose N_z=65 for both cases as shown in Table III. The flow field is fully developed when the magnetic field is on. We follow the same approach as Lyons, *et al*. [9] to get a realistic turbulent flow field. Start with a laminar flow profile with a disturbance on a coarse grid. Advance in time and allow the kinetic energy to redistribute from the (0, 0) mode to all of the higher modes. After the turbulent flow reaches a stationary state, the solution is interpolated onto a finer grid. The process is continued until the resolution is fine enough to pick up all scales of motion; the steady state solution at this resolution is used as the initial velocity field for the ferrofluid equations.

Before the full ferrohydrodynamic equations are solved, the channel code, for a Newtonian fluid at Re=2800, is verified and validated. The mean velocity results are validated against the empirical law-of-the-wall, and the directional energy spectra compares well with the published data of Moser, *et al.* [23].

G. *k-ε* model

The *k*-ε method of Chien [25] was also run for comparison, since it had been validated against fully developed turbulent channel flow data, including profiles of average velocity profiles, Reynolds stress, and turbulent kinetic energy. The parameters and functions used were for a low Reynolds number [26, Eq. 8] case, and the same parameters are used here for both Newtonian fluids and ferrofluids: $C_\mu = 0.09$, $C_{\varepsilon 1} = 1.35$, $C_{\varepsilon 2} = 1.8$, $\sigma_k = 1$, $\sigma_\varepsilon = 1.3$, and

$$f_\mu = 1 - \exp(-0.0115 z^+), \quad f_1 = 1, \quad f_2 = 1 - \frac{2}{9}\exp\left[-\left(\frac{R_T}{6}\right)^2\right]$$

$$D = \frac{2\upsilon k}{z^2}, \quad E = \left(-\frac{2\upsilon\varepsilon}{z^2}\right)\exp(-0.5 z^+), \quad R_T = \frac{k^2}{\upsilon\varepsilon}, \quad z^+ = (1-\frac{z}{\delta})Re_\tau$$

It is extended for ferrofluids using a model (but for channel flow) similar to that used in Schumacher, *et al.* [4] for pipe flow. The non-dimensional torque is

$$T_o = 0.5\chi_0\left[\frac{-\omega\tau_B(a+b^2)}{(a+b)^2 + (2+\chi_o)^2(\Omega\tau_B)^2}\right], a = (\omega\tau_B)^2 - (\Omega\tau_B)^2, b = 1 + \chi_o$$

The value of χ_o is taken as the slope of the magnetization versus magnetic field curve at the ξ in question, χ_o=0.1815, 0.0301 for H = 316, 948 Oe, respectively.

IV. RESULTS

A. Fractional Pressure Drop

Experiments show that when a slowly oscillating magnetic field, $\Omega\tau_B \ll 1$, is applied to turbulent ferrofluid pipe flow, the pressure drop required to maintain a constant flow rate increases [4]. The wall stress is related to the pressure drop by $\Delta P/L = \tau_w/\delta$. The Reynolds number based on wall stress is

$Re_\tau = \left(\sqrt{\tau_w/\rho}\, \delta \right) / \nu$. Figure 2 shows how Re_τ adjusts in time after the magnetic field is turned on. When the magnetic field is steady, the Re_τ readjusts to a new steady value, but when the magnetic field is oscillating, Re_τ has a more dynamic behavior and oscillates between the $\xi=0$ case and the case with $\xi=1.92$ (H = 316 Oe) and a steady magnetic field. The adjustment of the Re_τ to a steady state value occurs in approximately $1/10^{th}$ of a non-dimensional time unit. The fractional pressure drop (P_{FPD}) is computed at each time step in the simulation and time-averages are reported in Table IV. The pressure drop required to maintain a constant flow rate increases as the magnitude of the magnetic field goes up. The magnetic field has a larger effect when the Reynolds number is smaller. When the magnetic field oscillates, the pressure drop required to maintain a steady flow rate is between that for a steady field and no field. In fact, the fractional pressure drop oscillates between the values for the steady case and the zero field case. Thus, going from a steady to an oscillating magnetic field essentially reduces the effective viscosity.

The k-ε results are shown for comparison in Table IV and exhibit the same trends as the DNS, but the magnitude of the effect is larger in the k-ε solutions. When χ_o was calculated using the chord (M/H), (χ_o = 0.2705, 0.1425, for H = 316, 948 Oe, respectively) the fractional pressure drop was even larger and the errors were bigger. When the slope is used, as reported in Table IV, the k-ε model predicts results that are above the DNS results for H = 316 Oe and below them for H = 948 Oe. Both options for χ_o show very little change with frequency. While the k-ε model predicts the pressure drop with only a few percent error, the fractional pressure drop varies significantly from the DNS results. The trends shown here for channel flow, depending upon the magnetic field and frequency, agree with the trends measured for pipes in Ref. [4]. The fractional pressure drop varies most with magnetic field; in the k-ε model the fractional pressure drop does not change with frequency whereas it decreases very slightly as frequency is increased for the DNS model.

B. Mean profiles

The mean profiles of the velocity, turbulent kinetic energy, Reynolds stress, spin rate, and y-torque are plotted as a function of distance from the wall. The velocity is normalized by the friction

velocity based on total wall shear stress, $u_\tau = \sqrt{\tau_w/\rho}$. When the z^+ variable is used, it refers to $z^+ = (1-z)(u_\tau/\nu)$, otherwise z is normalized by the halfwidth, δ.

The mean velocity profiles are shown in Figure 3. As the magnetic field magnitude increases, there is a downward shift of the velocity profile in the log-region of the flow. The k-ε profiles show the same general behavior. The bulk average velocity is the same in all cases, but the velocity normalization factor, $u_\tau = \sqrt{\tau_w/\rho}$, changes with **H**. Figure 3c shows the same profile for a range of frequencies. The effect of frequency is very small.

The normalized turbulent kinetic energy is not largely affected by the steady magnetic field, as shown in Figure 4. The peaks occur at approximately the same z/δ value in all cases. The k-ε simulations show a good predictive capability, in that the profiles are similar and close together and the peaks occur at approximately the same place as the DNS data.

Figure 5 plots the normalized Reynolds stress vs. distance from the wall. In the DNS results, the Reynolds stress decreases as **H** is increased. In the k-ε simulations, the lines are almost superimposed. In the channel flow simulations, a constant flow rate is maintained by adjusting the applied pressure drop. As a result, the wall shear stresses at the upper and lower walls are no longer at fixed values. That is, $u_\tau(+\delta) \neq u_\tau(-\delta)$. Both $u_\tau(+\delta)$ and $u_\tau(-\delta)$ change in time. Thus, the spatially averaged vorticity and spin profiles are slightly asymmetric at any instant in time, but the profiles of vorticity and spin become symmetric when the spatially averaged profiles are time averaged over long times. Figure 5c shows that the effect of frequency is very slight. In Figure 6, the DNS results show that the mean spin profiles are highly asymmetric. As **H** increases, the spin decreases in both the DNS and the k-ε results.

The torque is a sensitive quantity, and is a non-linear function of the spin. In Figure 7, the mean y-torque is plotted for the two steady field cases. The torque from the k-ε model shows good agreement with the DNS torque.

C. Spectra

Next we examine the effect of steady magnetic fields on the energy spectra at $z^+\approx9$ and $z^+\approx150$ wall units from the wall. The Reynolds number is a constant 2250 for all the cases in this section. Figure 8 shows the effect of a steady magnetic field with a magnitude ξ=5.76 on the energy spectra at $z^+\approx9$ wall units. The magnetic field results, solid lines, are compared to the Newtonian results, dotted lines, for each case. The magnetic field has only a small damping effect on the spectra at high wave-numbers. Figure 9 shows the effect at the centerline, and the effect is minimal. For ξ=1.92 the curves are similar [16]. The figures show that there is no significant accumulation of energy at high wavenumbers, and that the energy at high wavenumbers is at least two or more decades lower than the energy at low wavenumbers. Thus, the grid resolution is adequate in the magnetic field simulations.

V. CONCLUSIONS

The pressure drop required to maintain a constant flow rate for a ferrofluid increases with the applied magnetic field strength. When a magnetic field is oscillated at a frequency of 1000 s^{-1} ($\Omega\tau_B$=0.06), the pressure drop required to maintain a constant flow rate is less than that when the magnetic field is steady, but larger than when there is no magnetic field applied. Applying the magnetic field has a bigger effect for smaller Reynolds numbers. The mean profiles involving velocity are not highly affected by magnetic field strength, but the spin and torque profiles show a strong dependence on **H**. The only significant change in energy spectra occurred near the wall in the case of a high magnetic field, ξ=5.76, where the spectra decreases slightly at large wavenumbers. The k-ε model does a reasonable job modeling the mean velocity profiles, the turbulent kinetic energy, Reynolds stresses, spin, and torque. The trends reported here for channel flow are very much in agreement with the experimental trends for pipe flow reported in Ref. [4]: in low Reynolds number turbulent flow the excess pressure drop increases with magnetic field and varies only slightly with frequency.

VI. ACKNOWLEDGMENTS

VII. REFERENCES

[1]. Tangthieng, C., Finlayson, B. A., Maulbetsch, J., Cader, T., J. Mag. Mag. Mat. **201** 252 (1999).

[2]. Crainic, M. S., Schlett, Z., J. Mag. Mag. Mat. **268** 8 (2004).

[3]. Frick, P., Khripchenko, S., Denisov, S., Sokoloff, D., Pinton, J.F., Eur. Phys. J. B. **25** 399 (2002).

[4] K. R. Schumacher, I. Sellien, G. S. Knoke, T. Cadar, and B. A. Finlayson, Phys. Rev. E **67**, 026308 (2003).

[5]. Zablockis, D., Frishfelds, V., Blums, E., Magnetohydrodynamics **45** 371 (2009).

[6] K. R. Schumacher, J. J. Riley, B. A. Finlayson, J. Fluid Mech. **599**, 1 (2008).

[7] K. R. Schumacher, J. J. Riley, B. A. Finlayson, Phys. Rev. E. **81** 016317 (2010).

[8] J. Kim, P. Moin, and R. Moser, J. Fluid Mech. **177**, 133 (1987).

[9] S. L. Lyons, T. J. Hanratty, and J. B. McLaughlin, Int. J. Num. Meth. Fluids **13**, 999 (1991).

[10] J. Rutledge and C. A. Sleicher, Int. J. Num. Meth. Fluids **16**, 1051 (1993).

[11] A. Gyr and A. Tsinober, J. Non-Newtonian Fluid Mech. **73**, 153 (1997).

[12] J. M. J. Den Toonder, M. A. Hulsen, G. D. C. Kuiken, and F. T. M. Nieuwstadt, J. Fluid Mech. **337**, 193 (1997).

[13] M. D. Warholic, H. Massah, and T. J. Hanratty, Exps. Fluids **27**, 461 (1999).

[14] M. I. Shliomis, Sov. Phys. JETP **34**, 1291 (1972).

[15] J. H. Ferziger, J. Comp. Physics **69**, 1 (1987).

[16] Schumacher, K. R., *Direct Numerical Simulation of Ferrofluid Turbulence in Magnetic Fields,* Ph. D. Thesis, University of Washington (2005).

[17]. Blums, E., A. Cebers, M. M. Maioro, *Magnetic Fluids*, Walter de Gruyter, Berlin (1997).

[18]. Lyubimov, D. V., and T. P. Lyubimova, Fluid Dyn. **19**, 907 (1984).

[19]. Shliomis, M. I., T. P. Lyubimova, and D. V. Lyubimov, Chem. Eng. Comm. **67**,275 (1988).

[20]. Tsebers, A. O., Magnetohydrodynamics **20**,343 (1984).

[21]. Felderhof, B. U. and H. J. Kroh, J. Chem. Phys. **110** 7403 (1999).

[22]. Martsenyuk, M. A., Y. L. Raikher, and M. I. Shliomis, Sov. Phys. JETP **38** 413 (1974).

[23] R. D. Moser, J. Kim, and N. N. Mansour, Phys. Fluids **11**, 943(1999).

[24] Kasagi, N., Tomita, Y. & Kuroda, A. ASME J. Heat Transfer **114**, 598 (1992).

[25] Chien, K.Y., AIAA J **20** 33 (1982).

[26] Henry, C. M., Bolio, E. J., Chakrabarti, D., Sinclair, J. L., Chem. Eng. Sci. **12** 1923 (1995).

N_z	Maximum Eigenvalue of **B**
33	$10^{4.7}$
40	$10^{5.08}$
65	$10^{5.9}$
97	$10^{6.6}$
129	$10^{7.1}$

Table I. Maximum Eigenvalues of B, for different Nz.

Case	Fluid	Re	H (Oe)	Ω(Hz)	Comments
A	Newtonian	2250	N/A	N/A	Initial cond. For cases B-G
B	Ferrofluid	2250	316, ξ=1.92	0	
C	Ferrofluid	2250	948, ξ=5.76	0	
D	Ferrofluid	2250	316, ξ=1.92	400	
E	Ferrofluid	2250	948, ξ=5.76	400	
F	Ferrofluid	2250	316, ξ=1.92	1000	
G	Ferrofluid	2250	948, ξ=5.76	1000	
H	Ferrofluid	2800	N/A	N/A	Initial cond. For cases B-G
I	Ferrofluid	2800	316, ξ=1.92	0	
J	Ferrofluid	2800	948, ξ=5.76	0	
K	Ferrofluid	2800	316, ξ=1.92	400	
L	Ferrofluid	2800	948, ξ=5.76	400	
M	Ferrofluid	2800	316, ξ=1.92	1000	
N	Ferrofluid	2800	948, ξ=5.76	1000	

Table II. Overview of the channel flow cases.

Re	2250	2800
Re_τ	~150	~180
Δt	6e-4	5e-4
$c_w=k^2$	0.25-5760	0.25-7585
c	$10^{5.699}$-$10^{5.704}$	$10^{5.857}$-$10^{5.862}$

Table III. Range of c and c_w.

				DNS Results			k-ε Results		
Case	H(Oe)	Ω(Hz)	Re	Re_τ	Re^*_τ	P_{FPD}	χ_0	Re^*_τ	P_{FPD}
A	0	0	2250	148.5765	148.5765	0	–	142.9247	0.0000
B	316	0	2250	148.5765	149.4596	0.01192	0.1815	143.8419	0.0129
C	948	0	2250	148.5765	153.1061	0.06190	0.0301	144.2930	0.0192
D	316	400	2250	148.5765	149.0662	0.00661	0.1815	143.8419	0.0129
E	948	400	2250	148.5765	151.3059	0.03718	0.0301	144.2940	0.0193
F	316	1000	2250	148.5765	149.0369	0.00621	0.1815	143.8421	0.0129
G	948	1000	2250	148.5765	151.1219	0.03466	0.0301	144.2943	0.0193
H	0	0	2800	182.1141	182.1141	0	–	172.2422	0.0000
I	316	0	2800	182.1126	182.6402	0.00579	0.1815	172.8321	0.0069
J	948	0	2800	182.1126	184.8629	0.03043	0.0301	173.1279	0.0103
K	316	400	2800	182.1127	182.4157	0.00332	0.1815	172.8322	0.0069
L	948	400	2800	182.1127	183.8142	0.01880	0.0301	173.1281	0.0103
M	316	1000	2800	182.1127	182.3845	0.00297	0.1815	172.8329	0.0069
N	948	1000	2800	182.1127	185.3628	0.01695	0.0301	173.1292	0.0103

Table IV. Summary of time-averaged results from DNS and comparison to Chien k-ε model.

FIG 1
(K. R. Schumacher, Phys. Rev. E)

FIG 2
(K. R. Schumacher, Phys. Rev. E)

FIG 3
(K. R. Schumacher, Phys. Rev. E)

Re=2250, Ω=0

(a)

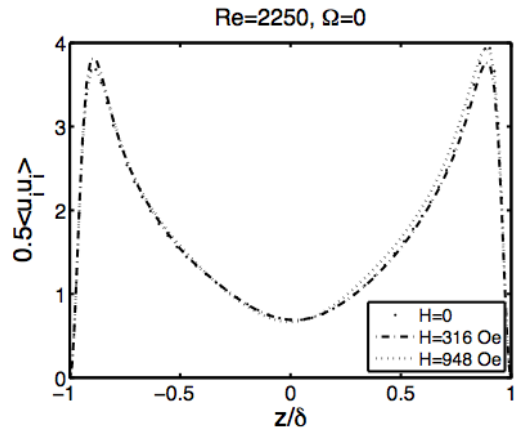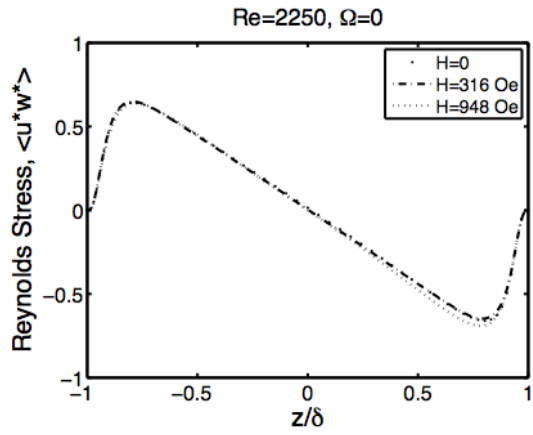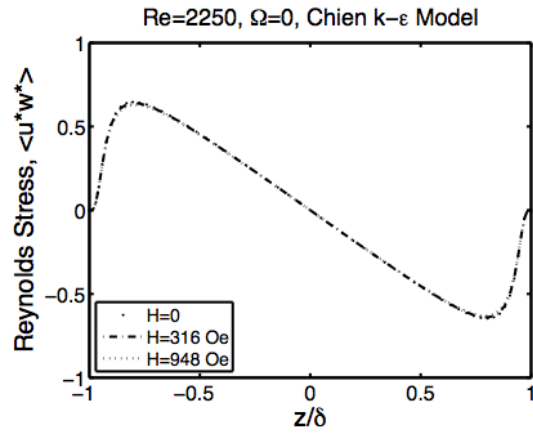Re=2250, Ω=0, Chien k–ε Model
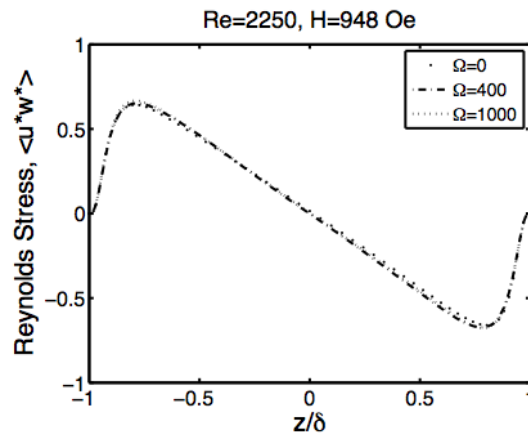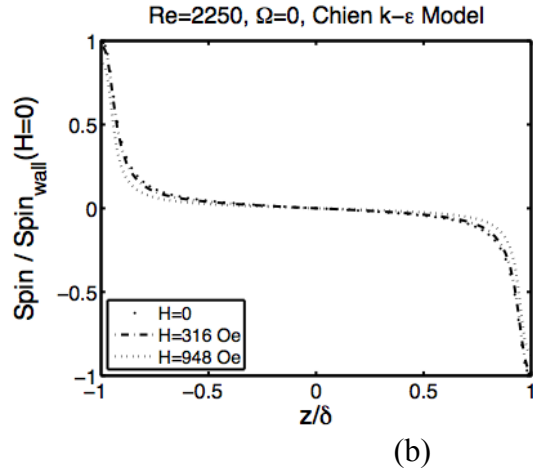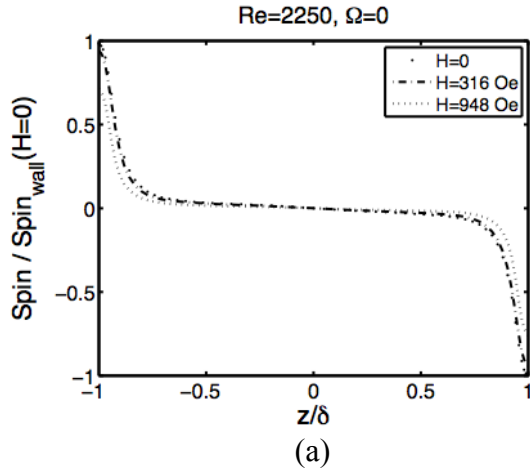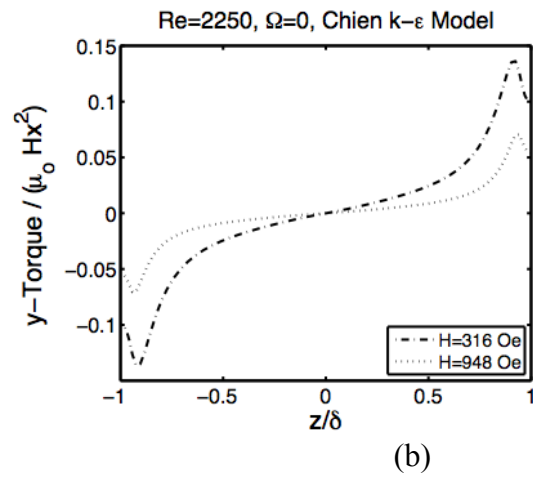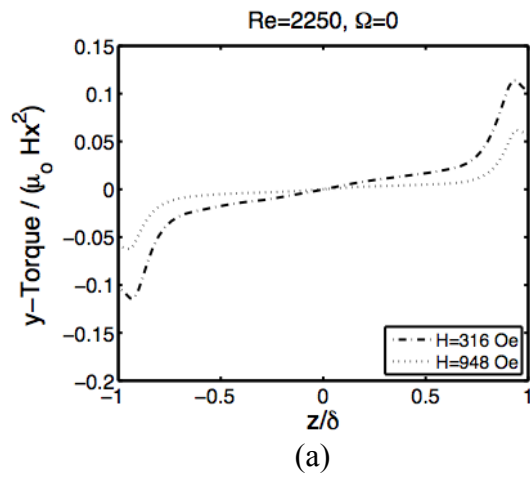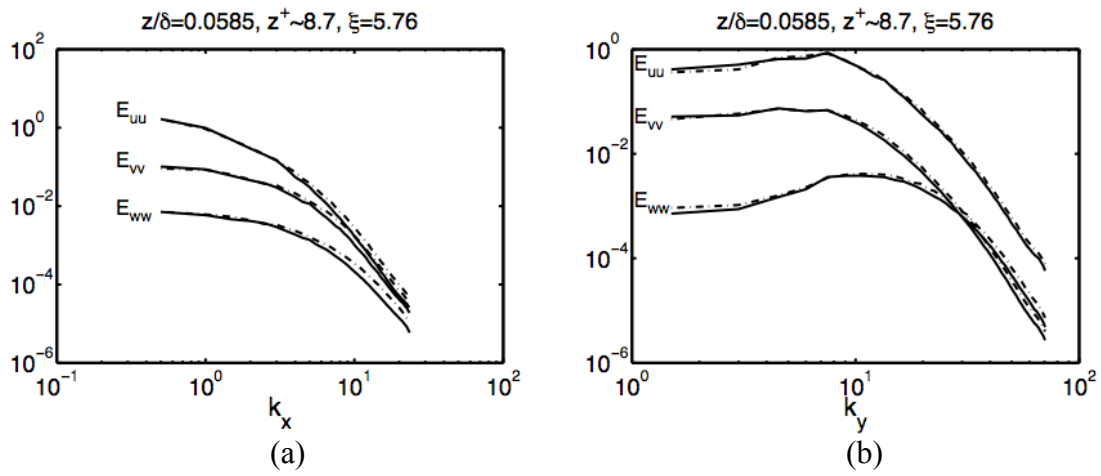
(b)
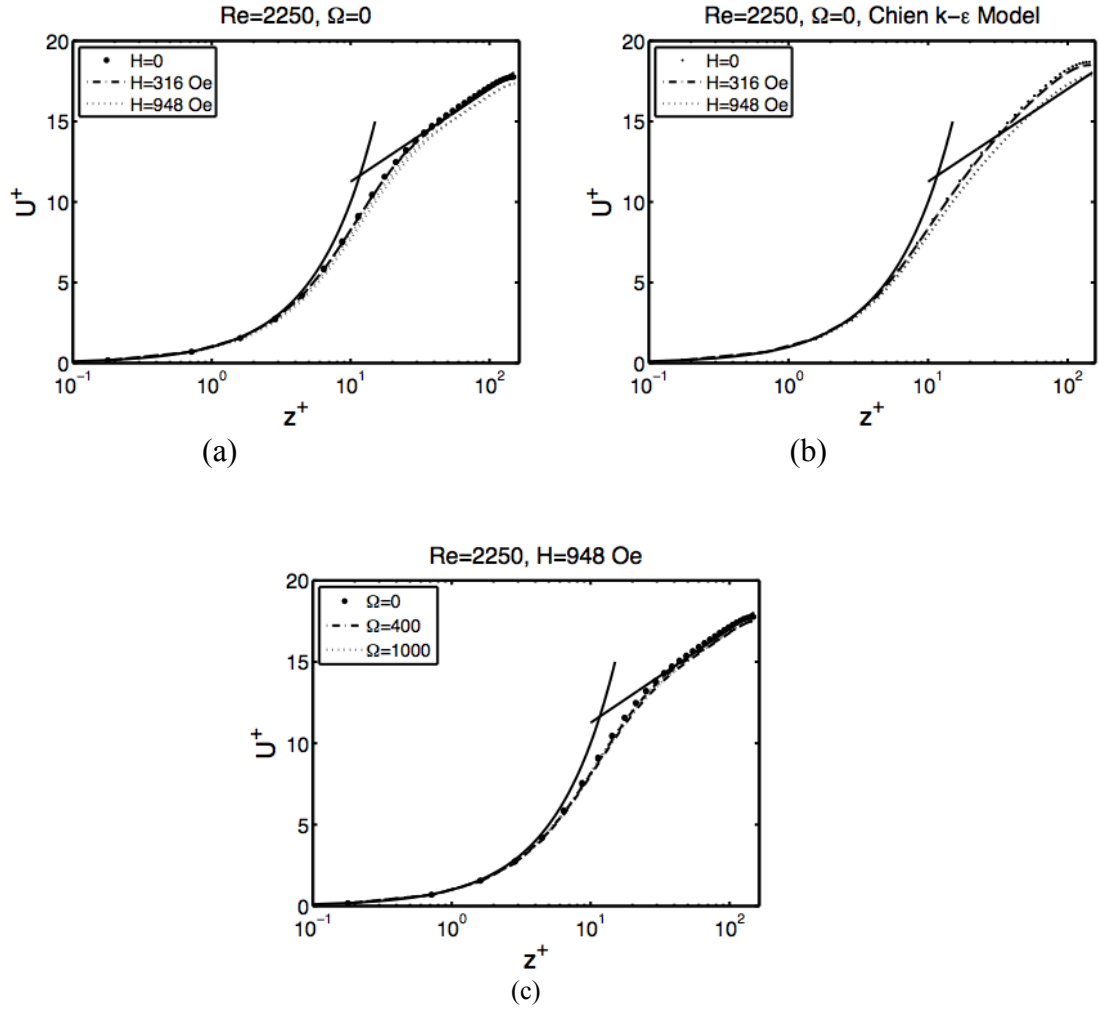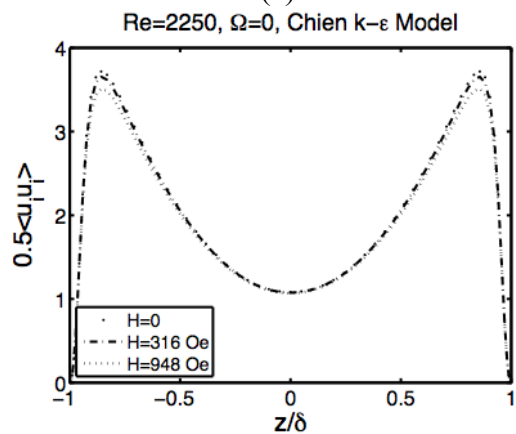
FIG 4
(K. R. Schumacher, Phys. Rev. E)

(a)

(b)

(c)

FIG 5
(K. R. Schumacher, Phys. Rev. E)

FIG 6
(K. R. Schumacher, Phys. Rev. E)

FIG 7
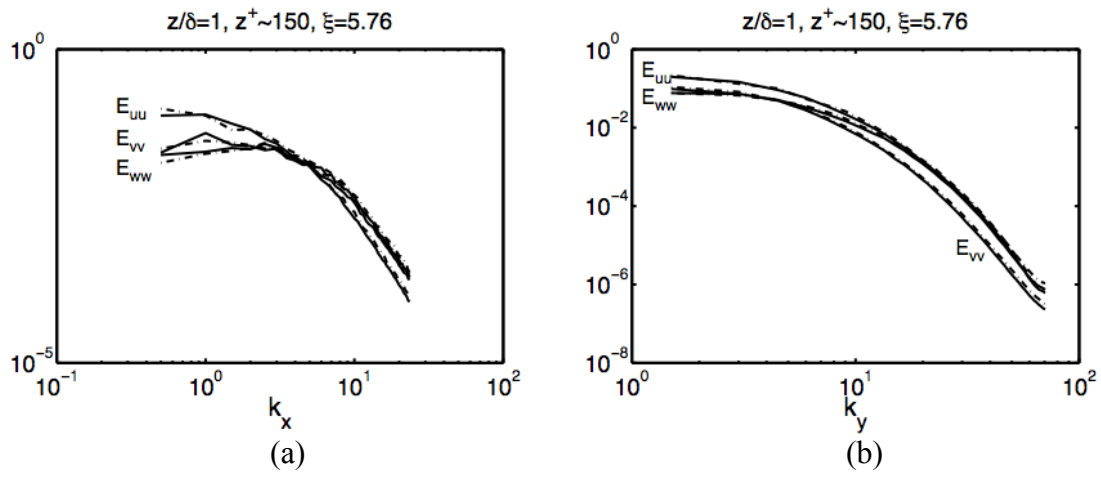(K. R. Schumacher, Phys. Rev. E)

FIG 8
(K. R. Schumacher, Phys. Rev. E)

FIG 9
(K. R. Schumacher, Phys. Rev. E)